LAPPED-WINDOWED RECONSTRUCTIONS IN COMPRESSIVE SPECTRAL IMAGING

by

Claudia V. Correa-Pugliese

A thesis submitted to the Faculty of the University of Delaware in partial fulfillment of the requirements for the degree of Master of Science in Electrical and Computer Engineering

Spring 2013

LAPPED-WINDOWED RECONSTRUCTIONS IN COMPRESSIVE SPECTRAL IMAGING

by

Claudia V. Correa-Pugliese

Approved: ______________________________

Gonzalo R. Arce, Ph.D.
Professor in charge of thesis on behalf of the Advisory Committee

Approved: ______________________________

Kenneth E. Barner, Ph.D.
Chair of the Department of Electrical and Computer Engineering

Approved: ______________________________

Babatunde Ogunnaike, Ph.D.
Interim Dean of the College of Engineering

Approved: ______________________________

James G. Richards, Ph.D.
Vice Provost for Graduate and Professional Education

TABLE OF CONTENTS

LIST OF TABLES

LIST OF FIGURES

ABSTRACT

Traditional spectral imaging techniques scan the whole region of interest to obtain a three dimensional set that contains the spatial and spectral information of the scene. In contrast, compressive spectral imaging systems allow capturing the spatial and spectral information of the scene using two dimensional sets of random projections. These systems rely on the theory of compressed sensing (CS), which establishes that certain signals can be recovered with high probability using far fewer samples from those dictated by Nyquist. The coded aperture snapshot spectral imaging system (CASSI) is an optical imaging architecture that accomplishes compressive spectral imaging. The reconstruction of the scene is obtained by ℓ_1 norm based inverse optimization algorithms such as the gradient projections for sparse reconstruction (GPSR). The computational complexity of the inverse problem grows with order $O(KN^4L)$ per iteration, where N^2 and L are the spatial and spectral dimensions of the scene, respectively, and K is the number of snapshots. Many applications deal with high-dimensional spectral images, and the computational complexity becomes overwhelming since reconstructions can take up to several hours in desktop architectures. The goal of this thesis is to obtain a mathematical model for block reconstructions in CASSI, such that the reconstruction quality is not affected and the computational complexity is reduced. The results obtained show that the lapped block reconstruction model in CASSI satisfies the premises with complexity $O(NB^4L)$ per GPSR iteration, where $B \ll N$ is the block size. The proposed approach takes advantage of the structure of the transfer function of the CASSI system thus allowing the independent recovery of small lapped blocks of the measurement set. A merging process to reduce the blocking artifacts in the reconstructed scene is also described. Simulations show the benefits of the new

model in terms of PSNR and reconstruction time. In particular, the data cube reconstruction can be accelerated by an order of magnitude and the PSNR is improved up to 5 dB over traditional reconstruction approach.

Chapter 1

INTRODUCTION

Spectral imaging involves both Spectroscopy and Imaging [17]. Imaging is related to the acquisition of spatial and temporal data from a scene and, spectroscopy allows the description of phenomena occurred in data sets containing light intensities at different wavelengths, usually called spectrums. Spectral imaging provides signals that include both spatial and spectral information in a single data set. Since this type of images consists of 3-dimensional sets, they can be represented as data cubes with one spectral dimension and two spatial dimensions. This representation is illustrated in Fig.1.1.

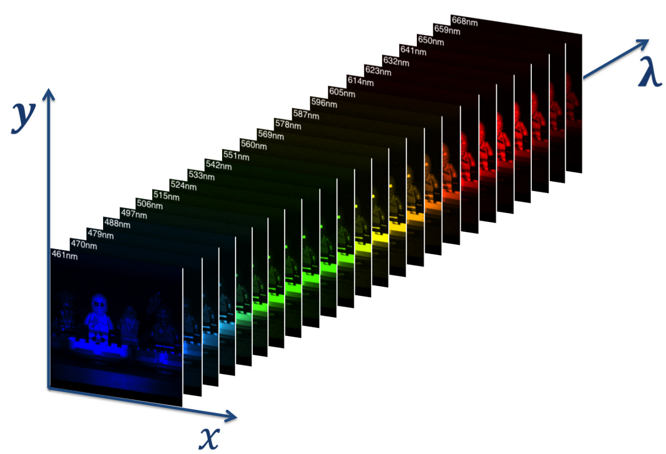

Figure 1.1: Spectral Image data set where x and y correspond to the spatial dimensions and λ is the spectral dimension. Each spatial point in the image contains a full spectrum $I(x, y, \lambda)$.

Spectral images are mainly used in applications involving material identification, anomaly detection, and remote sensing of the environment [30]. More specifically, objects in a scene can be detected and classified using their spectrum by exploiting the fact that different materials exhibit different spectral signatures according to their molecular composition, scale and shape [28, 35, 10]. Other applications of spectral images include analysis of artwork for restoration purposes [15, 24, 21], medical applications and microscopy [19, 18].

Conventional spectral imaging techniques such as pushbroom [19] and whiskbroom [20], scan the scene along one or two dimensions and then capture the data along the remaining dimensions to obtain the data cube. In particular, a pushbroom imaging sensor scans the scene line by line, while a whiskbroom sensor scans pixel by pixel. The disadvantage of these techniques is that the collected amount of data is linearly proportional to the desired spatial and spectral resolutions [8, 33].

Compressive spectral imaging senses the spatio-spectral information of a scene using a small set of 2-Dimensional (2D) focal plane array (FPA) measurements. The reconstruction of the 3D spectral scene is obtained via compressive sensing inverse algorithms which exploit a sparse representation of the data cube. Let a hyperspectral signal $\mathbf{F} \in \mathbb{R}^{N \times N \times L}$, or its vectorized representation $\mathbf{f} \in \mathbb{R}^{N^2 L}$, be represented in the basis $\mathbf{\Psi}$. A sparse approximation of $\mathbf{f}$ is such that $\mathbf{f} = \mathbf{\Psi}\boldsymbol{\theta}$ can be accurately represented as a linear combination of $S \ll N^2L$ vectors of $\mathbf{\Psi}$. Compressive spectral imaging dictates that $m \gtrsim S \log{(N^2L)} \ll N^2L$ random measurements are sufficient for the recovery of $\mathbf{f}$ with high probability. The coded aperture snapshot spectral imager (CASSI) is an architecture that accomplishes compressive spectral imaging measurements [33]. The spectral image scene is projected onto FPA measurements as linear combinations of coded and shifted versions of the spectral channels of the underlying signal. A single FPA measurement in CASSI is represented by $\mathbf{y} = \mathbf{Hf}$ where $\mathbf{H}$ is a $N(N+L-1) \times (N^2L)$ matrix that accounts for the effects of the coded aperture and the dispersive element [3]. In practice, several FPA projections are captured, each one using a different coded aperture pattern. The multi-frame approach improves the conditioning of the inverse reconstruction problem, making the CASSI system more suitable for applications involving spectrally or spatially rich scenes [2, 4]. Multiple coded aperture patterns can be realized by a piezo system [23] or using a digital micromirror device (DMD) [37, 6]. The compressive projections on the i^{th} snapshot are given by $\mathbf{y}^i = \mathbf{H}^i\mathbf{f}$. The ensemble of outputs for K snapshots $\mathbf{y} = \left[(\mathbf{y}^0)^T, \ldots, (\mathbf{y}^{K-1})^T\right]^T$ can be expressed as $\mathbf{y} = \mathbf{H}\mathbf{f}$ where $\mathbf{H} = \left[(\mathbf{H}^0)^T, \ldots, (\mathbf{H}^{K-1})^T\right]^T$. The theory of compressed sensing is then used to reconstruct the underlying signal $\mathbf{f} = \boldsymbol{\Psi}\boldsymbol{\theta}$.

Several numerical algorithms are available to solve the reconstruction problem, and can be grouped into one of five computational approaches [32]. Algorithms based on greedy pursuit iteratively find an estimate of the solution by selecting atoms of a dictionary and the correspondent weighting factors such that the signal can be represented as a linear combination of these vectors. This approach is implemented by algorithms such as the Orthogonal Matching Pursuit (OMP) [31], stagewise orthogonal matching pursuit (StOMP) [11], and compressive sampling matching pursuit (CoSaMP) [26]. The second type of algorithms consists of those that solve a convex optimization problem. This includes interior-point methods such as ℓ_1-magic software and gradient-descent methods like the sparse reconstruction via separable approximation (SpaRSA) [36], TwIST [7] and GPSR [14]. The third approach uses a Bayesian framework which finds a maximum a posteriori estimator assuming a prior distribution of the unknown coefficients of the signal to recover [29]. The other two techniques are nonconvex optimization [9] and brute force, which attempts to find the solution by trying all possible support sets. A tutorial review of the algorithms in each of these class-types and their associated complexity is found in [32]. Some of these algorithms exhibit better characteristics than others in terms of computational complexity. Typical computations performed by these algorithms include matrix pseudo inverses, sparse basis transformations, scalar-vector multiplications, and vector-matrix multiplications.

Given that the underlying signals are high dimensional, these calculations require a large number of float point operations. Our work builds on the GPSR algorithm which has provided a good trade-off between computational complexity and reconstruction quality. The methods developed here are general and can thus be used with other reconstruction algorithms. In each iteration of the GPSR algorithm, approximately $O(KN^4L)$ operations are computed where K is the number of measurement shots, N is the spatial dimensions, and L is the number of spectral channels of the data cube. Reconstructions of large scenes are indeed overwhelming since they can take hours in desktop architectures [34, 23].

Previous work in compressive sensing (CS) have addressed this issue by working with separable sensing operators [27, 12, 16], or fast FPGA and GPU implementations of the reconstruction algorithms [13]. Instead of relying on hardware solutions, the methods developed in this paper aim at mitigating the computational complexity by exploiting the physical properties of the CASSI optical sensing phenomena. In particular, we reconstruct the underlying 3 dimensional scene from a set of reconstructions obtained from overlapping windowed FPA measurements. The block model developed is such that the overlapped parallelepiped regions of the underlying signal $\mathbf{f}$ are recovered independently. In this manner, the GPSR reconstruction algorithm performs $O(KB^4L)$ operations per iteration on each $B \times B$ block reconstruction with $KB^4L \ll KN^4L$. After recovery, the new model permits assembling the individual parallelepipeds to construct the complete data cube.

The contents of this thesis are organized as follows. First, a description of the mathematical model of the CASSI system is presented. There, the structure of the sensing matrix $\mathbf{H}$ is described. The block reconstruction model with non-overlapping and lapped windows are introduced subsequently. The block size and the overlapping sections are analyzed as a function of the number of shots and the spatial dimensions of the data cube. Extensive simulations show the improvements on the recovered spectral images in terms of PSNR and time for reconstruction with respect to the traditional approach of recovering the data cube at once. The reconstruction is thus analyzed using three models: the conventional multi-frame CASSI approach, a block CASSI model, and a lapped block CASSI model. The reconstruction of the data cube $\hat{\mathbf{F}}$ is then described for each model. It will be shown that the use of lapped measurement windows allows both, faster reconstructions and improved reconstruction quality.

Chapter 2

BACKGROUND: MULTI-FRAME CODED APERTURE SNAPSHOT SPECTRAL IMAGING (CASSI)

The Coded Aperture Snapshot Spectral Imaging system is an architecture that captures the spatial and spectral information from a scene in a set of 2D measurements. The projections in CASSI are attained using a coded aperture and a dispersive element [33]. The principal components in CASSI are illustrated in Fig. 2.1.

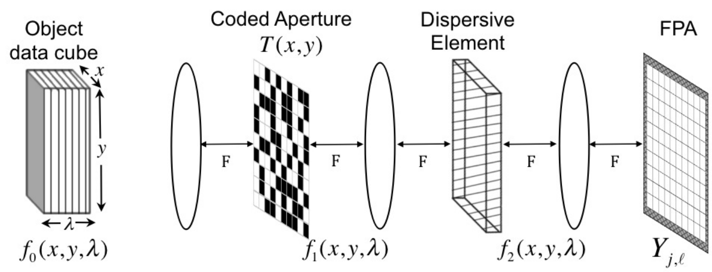

Figure 2.1: CASSI architecture. The input signal $f_0(x, y, \lambda)$ is coded by the coded aperture $T(x, y)$ and dispersed by the prism. The coded and dispersed signal $f_2(x, y, \lambda)$ is integrated on the FPA detector.

The underlying analog phenomena in CASSI is often discretized for analysis and computational purposes. In particular, the spatio-spectral input signal $f_0(x, y, \lambda)$ is represented by $F_{j\ell k}$ where j, ℓ index the spatial axes and k indexes the spectral axis λ. The coded aperture $T(x, y)$ is also discretized as $T_{j\ell}$, and a band-pass filter in the instrument limits the spectral components between λ_0 and λ_L.

A single shot measurement in CASSI is depicted in Fig. 2.2. A discretized data cube with L spectral bands $\mathbf{F} = [\mathbf{F}_0, \cdots, \mathbf{F}_{L-1}]$ is first coded in amplitude by the coded aperture $\mathbf{T}^i$. The effect of the dispersive element is depicted in Fig. 2.2 as a spatial shifting of each spectral band. The coded and dispersed information is integrated along the spectral axis at the detector. The i^{th} FPA measurement yields $N \times (N + L - 1)$ pixels as [33]

$$Y^i_{j\ell} = \sum_{k=0}^{L-1} F_{j(\ell+k)(k)} T^i_{j(\ell+k)} + \omega^i_{j\ell} \quad i = 0, \ldots, K-1. \tag{2.1}$$

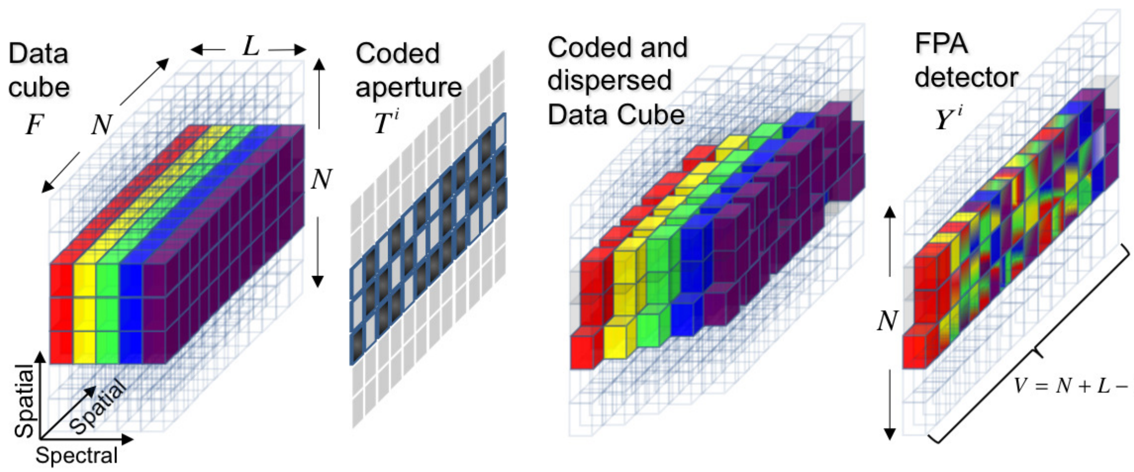

Figure 2.2: The process of CASSI imaging is depicted. A $N \times N \times L$ spectral data cube is spatially coded by the coded aperture and dispersed by the prism. Each pixel at the detector contains the integration of the spectral information from the correspondent entries of the data cube.

A vectorized representation of $\mathbf{Y}^i$ in Eq. 2.1 can be obtained as

$$\left(\mathbf{y}^i\right)_\ell = Y^i_{(\ell - rN)r} \qquad \text{for} \quad \ell = 0, \cdots, M-1, \quad i = 0, \cdots, K-1 \tag{2.2}$$

where $r = \lfloor \frac{\ell}{N} \rfloor$ and $M = N(N + L - 1)$. The data cube $\mathbf{F}$ is also represented in vector form as $\mathbf{f} = \left[\mathbf{f}_0^T, \cdots, \mathbf{f}_{L-1}^T\right]^T$ where each spectral band $\mathbf{f}_k$ can be expressed as $\mathbf{f}_k = \left[F_{00k}, F_{10k}, \cdots, F_{(N-1)0k}, \cdots, F_{01k}, F_{11k}, \cdots, F_{(N-1)1k}, \cdots, F_{(N-1)(N-1)k}\right]^T$. A compact vectorized representation of $\mathbf{f}_k$ is given by

$$\left(\mathbf{f}_k\right)_\ell = F_{(\ell - rN)rk} \qquad \text{for} \quad \ell = 0, \cdots, N^2-1, \quad k = 0, \cdots, L-1 \tag{2.3}$$

where $r = \lfloor \frac{\ell}{N} \rfloor$. The vectorized representation of the i^{th} coded aperture $(\mathbf{t}^i)_\ell$ is obtained using the indexing described in Eq. 2.2. These vector representations are then used to derive the single shot matrix model for CASSI

$$\mathbf{y}^i = \mathbf{H}^i \mathbf{f} + \boldsymbol{\omega}^i \tag{2.4}$$

in which the matrix $\mathbf{H}^i$ accounts for the coded apertures and the dispersive element effects. The sensing matrix for a single measurement shot is then given by

$$\mathbf{H}^i = \left[\begin{array}{ccc|ccc|c|ccc}
\mathbf{t}^i_{00} & & & & \mathbf{0}_{N(1)\times N^2} & & \cdots & & \mathbf{0}_{N(L-1)\times N^2} & \\
 & \ddots & & \mathbf{t}^i_{00} & & & & & & \\
 & & \mathbf{t}^i_{(N-1)(N-1)} & & \ddots & & \cdots & \mathbf{t}^i_{00} & & \\
 & & & & & \mathbf{t}^i_{(N-1)(N-1)} & & & \ddots & \\
 & \mathbf{0}_{N(L-1)\times N^2} & & & \mathbf{0}_{N(L-2)\times N^2} & & \cdots & & & \mathbf{t}^i_{(N-1)(N-1)}
\end{array}\right] \tag{2.5}$$

where $\mathbf{0}_{N(1)\times N^2}$ and $\mathbf{0}_{N(L-1)\times N^2}$ are $N(1)\times N^2$ and $N(L-1)\times N^2$ zero-valued matrices, and the non-zero entries in $\mathbf{H}$ correspond to $\text{diag}\,(\mathbf{t}^i)$, a $N^2 \times N^2$ diagonal matrix whose entries are the elements of the vectorized coded aperture $\mathbf{t}^i$, respectively. When several measurement shots are available, their outputs can be assembled in a single vector as $\mathbf{y} = \left[(\mathbf{y}^0)^T, \cdots, (\mathbf{y}^{K-1})^T\right]^T$ and the CASSI model for multiple shots [4, 23] can be written as

$$\mathbf{y} = \mathbf{H}\mathbf{f} + \boldsymbol{\omega} \tag{2.6}$$

where $\mathbf{H} = \left[(\mathbf{H}^0)^T, \cdots, (\mathbf{H}^{K-1})^T\right]^T$. Figure 2.3 shows an example of the matrix $\mathbf{H}$ for $N = 4$, $L = 3$, and $K = 2$. It can be noticed that the matrix $\mathbf{H}$ in Eq. 2.5 is sparse and highly structured. Each row contains at most L non-zero elements. A summary of the variables in CASSI model is shown in Table 2.1.

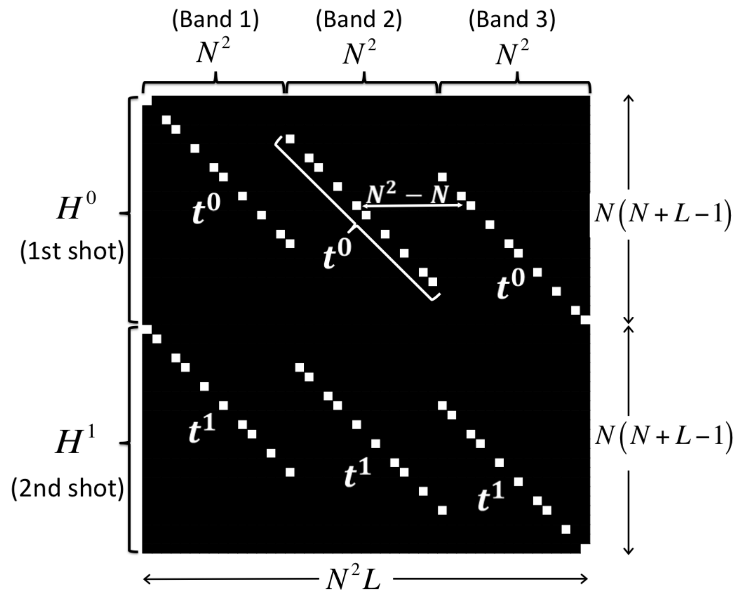

Figure 2.3: Structure of the matrix $\mathbf{H}$ for $N = 4$, $L = 3$ and $K = 2$.

The set of FPA measurements $\mathbf{y}$ in Eq. 2.6 is used as an input to the reconstruction algorithm (GPSR) to recover the entire data cube $\hat{\mathbf{F}} = \left[\hat{\mathbf{F}}_0, \cdots, \hat{\mathbf{F}}_{L-1}\right]$ at once, where $\hat{\mathbf{F}}_k$ is the reconstruction of the k^{th} spectral band. The underlying signal is obtained by solving $\hat{\mathbf{f}} = \mathbf{\Psi}\left(\underset{\boldsymbol{\theta}}{\operatorname{argmin}}||\mathbf{y} - \mathbf{H}\mathbf{\Psi}\boldsymbol{\theta}||_2 + \tau||\boldsymbol{\theta}||_1\right)$, where $\boldsymbol{\theta}$ is an S-sparse representation of $\mathbf{f}$ on the basis $\mathbf{\Psi}$ and τ is a regularization constant.

The computational complexity per GPSR iteration is described in [14]. It is determined by inner products, vector-scalar multiplications, and vector additions, each requiring N^2L floating-point operations, plus sparse basis transformations and multiplications by $\mathbf{H}$ and $\mathbf{H}^T$. Fast wavelet transform algorithms compute N^2L operations, and the cost of multiplying by $\mathbf{H}$ and $\mathbf{H}^T$ is determined by the matrix size $N(N + L - 1) \times N^2L$ which is on the order of N^4L. If K measurement snapshots are taken, the computational complexity is in the order of $O\left(KN^4L\right)$ per GPSR iteration.

One approach to simplify the CASSI reconstruction is to recover one slice $\hat{\mathbf{F}}_{j_1\ell k}$ of the data cube at a time, for $\ell = 0, \cdots, N-1$, $k = 0, \cdots, L-1$ and a fixed j_1. This is possible as the compressive measurements are coded along the x direction only due

Table 2.1: CASSI model variables

Variable	Size	Description
L		Number of spectral bands
$N \times N$		Spatial dimensions of the data cube
K		Number of measurement shots
$\mathbf{F} = [\mathbf{F}_0, \cdots, \mathbf{F}_{L-1}]$	$N \times N \times L$	Data cube
$\mathbf{f} = \left[\mathbf{f}_0^T, \cdots, \mathbf{f}_{L-1}^T\right]^T$	$N^2 L$	Vectorized form of $\mathbf{F}$
$\mathbf{T}^i$	$N \times N$	Coded aperture used in the i^{th} shot
$\mathbf{t}^i$	N^2	Vectorized form of $\mathbf{T}^i$
$\mathbf{Y}^i$	$N \times (N + L - 1)$	CASSI output from the i^{th} shot
$\mathbf{y}^i$	$N(N + L - 1)$	Vectorized form of $\mathbf{Y}^i$
$\mathbf{y} = \left[(\mathbf{y}^0)^T, \cdots, (\mathbf{y}^{K-1})^T\right]^T$	$KN(N + L - 1)$	Vectorized form of K CASSI outputs
$\mathbf{H}^i$	$N(N + L - 1) \times N^2 L$	CASSI matrix for the i^{th} shot
$\mathbf{H} = \left[\left(\mathbf{H}^0\right)^T, \cdots, \left(\mathbf{H}^{K-1}\right)^T\right]^T$	$KN(N + L - 1) \times N^2 L$	CASSI matrix for K shots

to the prism dispersion. The drawback however, is that the 3D basis modeling is then not utilized leading to poor signal reconstruction. The block approach to be described next, overcomes these limitations.

Chapter 3

BLOCK RECONSTRUCTION MODEL

The block-model of CASSI exploits the structure of the sensing matrix for recovering the underlying data cube from a set of reconstructions attained from smaller windowed FPA measurements. The windowed observations can be non-overlapping or lapped. In this approach, the CASSI sensing process is not modified, but a different reconstruction methodology is used. A detailed analysis of the relation between the elements of the sensing matrix $\mathbf{H}$ and the set of random projections in the detector is first developed. The reconstruction of the data cube from the set of windowed reconstructions is then described.

3.1 Decomposition of the Measurement Set

In this model, the measurement set is decomposed into non-overlapped windows. Consider a $B \times B$ measurement window of the FPA $\mathbf{Y}^i_{m,n}$, as shown in Fig. 3.1, and let's trace the energy in the window back through the optical system. After the prism, the energy collected by the $B \times B$ FPA window is a coded and dispersed square cube source with L spectral bands. The corresponding energy that is traced back to the source is no longer a cube but an oblique parallelepiped consisting of L spectral bands, each one shifted one spatial position in the horizontal axis. Figure 3.1 illustrates how an oblique parallelepiped block of the data cube, which is amplitude modulated by a coded aperture of size $B \times (B + L - 1)$ and spectrally sheared by the prism, results on a $B \times B$ block of measurements at the detector. In other words, the voxels that are sensed in a $B \times B$ area of the detector emanate from an oblique volume in the source and not from a cube. Furthermore, the oblique parallelepiped volume, once it is sheared by the prism, is transformed into a $B \times B$ cube before it impinges onto the detector.

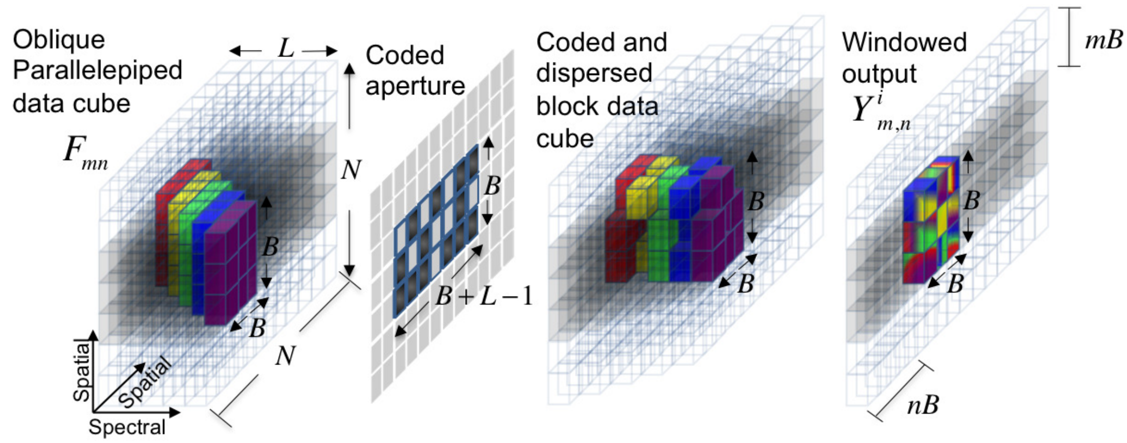

Figure 3.1: Each $B \times B$ window at the detector results from sensing a $B \times B \times L$ oblique parallelepiped block of the data cube. The CASSI sensing process is not modified.

The energy impinging on an adjacent window at the FPA can be traced back to the source in a similar manner, such that entire FPA measurement $\mathbf{Y}^i \in \mathbb{R}^{N\times(N+L-1)}$ can be expressed as an $N' \times V'$ ensemble of $B \times B$ windows as

$$\mathbf{Y}^i = \begin{bmatrix} \mathbf{Y}^i_{0,0} & \mathbf{Y}^i_{0,1} & \cdots & \mathbf{Y}^i_{0,V'-1} \\ \vdots & \vdots & \ddots & \vdots \\ \mathbf{Y}^i_{N'-1,0} & \mathbf{Y}^i_{N'-1,1} & \cdots & \mathbf{Y}^i_{N'-1,V'-1} \end{bmatrix} \tag{3.1}$$

where the set of $\mathbf{Y}^i_{m,n}$ matrices are non-overlapping blocks of $\mathbf{Y}^i$. The total number of blocks in the set is $N' = \frac{N}{B}$ and $V' = \lceil \frac{N+L-1}{B} \rceil$, with B determining the block size used in the new model. More on the selection of B will be described shortly.

Now consider the sensing process of one parallelepiped block of the data cube, expressed in vectorial form as

$$\mathbf{y}^i_{mn} = \mathbf{H}^i_{mn}\mathbf{f}_{mn} + \boldsymbol{\omega}^i_{mn} \tag{3.2}$$

where $(\mathbf{y}^i_{mn})_\ell = (Y^i_{mn})_{(\ell - rB)r}$ for $\ell = 0, \cdots, B^2 - 1$, $i = 0, \cdots, K-1$ and $r = \lfloor \frac{\ell}{B} \rfloor$. The parallelepiped volume in the data cube can be expressed in matrix form as

$$(\mathbf{F}_{mn})_{j,\ell,k} = (\mathbf{F})_{mB+j+1, nB+\ell+k+1, k} \tag{3.3}$$

for $k = 0, \cdots, L-1$ and $j, \ell = 0, \cdots, B-1$. Hence, $\mathbf{f}_{mn}$ in Eq. 3.2 is a vectorized representation obtained as $(\mathbf{f}_{mnk})_\ell = (F_{mn})_{(\ell - rB)rk}$ where $\ell = 0, \cdots, B^2 - 1$, $k = 0, \cdots, L-1$ and $r = \lfloor \frac{\ell}{B} \rfloor$. The matrix $\mathbf{H}^i_{mn}$ in Eq. 3.2 is a $B^2 \times B^2 L$ sub-matrix of $\mathbf{H}^i$ obtained by choosing the rows and columns that affect each windowed FPA measurement. More specifically, the (ℓ, j) element in the (m, n) sub-matrix is given by

$$\left(\mathbf{H}^i_{mn}\right)_{\ell,j} = \left(\mathbf{H}^i\right)_{r_\ell, r_j} \tag{3.4}$$

where $r_\ell = (nB + \alpha) N + mB + \ell - B\alpha + 1$ and $r_j = r_\ell + u(N^2 - N)$. Fig. 3.2 illustrates the procedure used to obtain the $\mathbf{H}^i_{mn}$ sub-matrices from $\mathbf{H}^i$. Here, a portion of the matrix in Fig. 2.3 is shown and, six sub-matrices are obtained from $\mathbf{H}^i$ for $N = 4$, $L = 3$ and $B = 2$. Accordingly $N' = 2$ and $V' = 3$. The colors of the non-zero values are intended to identify the elements that correspond to each sub-matrix.

The set of windowed measurements from sequential FPA shots can then be assembled as in the CASSI model to obtain $\mathbf{y}_{mn} = \left[\left(\mathbf{y}^0_{mn}\right)^T, \cdots, \left(\mathbf{y}^{K-1}_{mn}\right)^T \right]^T$ and the correspondent matrices $\mathbf{H}^i_{mn}$ are assembled as $\mathbf{H}_{mn} = \left[\left(\mathbf{H}^0_{mn}\right)^T, \cdots, \left(\mathbf{H}^{K-1}_{mn}\right)^T \right]^T$. Thus, the multi-shot non-overlapping block CASSI model can be rewritten as

$$\mathbf{y}_{mn} = \mathbf{H}_{mn} \mathbf{f}_{mn} + \boldsymbol{\omega}_{mn}. \tag{3.5}$$

Notice that in this model, the matrices in Eq. 3.4 preserve the structure of $\mathbf{H}^i$ in Eq. 2.5 with dimensions considerably smaller. The number of non-zero elements in the complete CASSI sensing matrix is KN^2L when K measurement shots are taken. For the same number of shots in the block model, each matrix has at most KN^2L/C^2

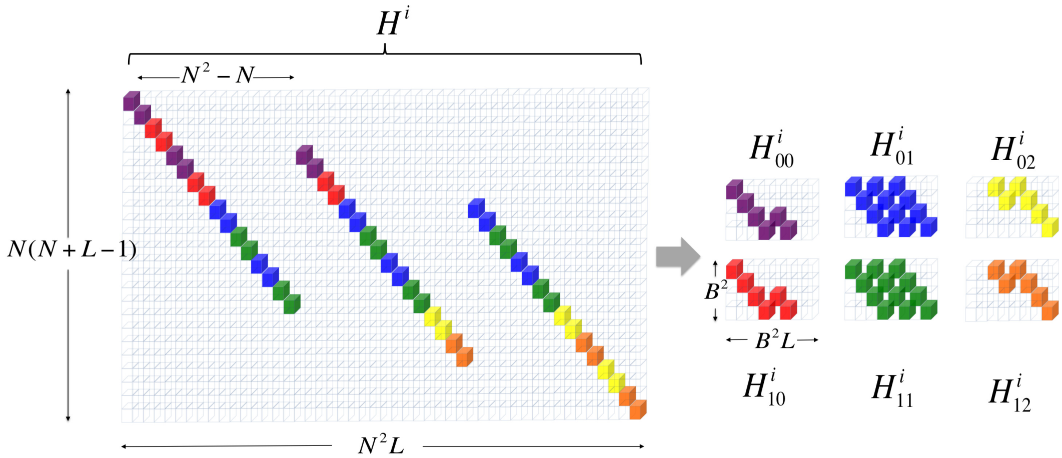

Figure 3.2: Procedure to obtain the $\mathbf{H}^i_{mn}$ matrices from $\mathbf{H}^i$ for $N = 4$, $L = 3$ and $B = 2$. The non-zero elements are colored, where each color corresponds to a different sub-matrix $\mathbf{H}^i_{mn}$. The resultant $B^2 \times B^2L$ matrices are obtained by selecting the correspondent rows for each block and removing the zero-valued columns.

non-zero elements with $C = \frac{N}{B}$.

3.2 Data Cube Reconstruction from Non-overlapping Measurement Windows

Each individual set of windowed measurements $\mathbf{y}_{mn}$ from Eq. 3.5 is now inputted to the GPSR algorithm to recover an oblique parallelepiped $\hat{\mathbf{F}}_{mn} \in \mathbb{R}^{B \times B \times L}$ within the data cube. More specifically, a vectorized representation of the underlying signal $\hat{\mathbf{F}}_{mn}$ is recovered by solving

$$\hat{\mathbf{f}}_{mn} = \boldsymbol{\Psi}' \left(\underset{\boldsymbol{\theta}'}{\operatorname{argmin}} ||\mathbf{y}_{mn} - \mathbf{H}_{mn}\boldsymbol{\Psi}'\boldsymbol{\theta}'||_2 + \tau||\boldsymbol{\theta}'||_1 \right) \tag{3.6}$$

where $\boldsymbol{\theta}'$ is a sparse representation of $\hat{\mathbf{f}}_{mn}$ in the basis $\boldsymbol{\Psi}'$. It can be noticed that the inverse problem for the block reconstruction is the same as that in the traditional approach. However, the sensing matrix in the block reconstruction $\mathbf{H}_{mn}$ is a portion of the complete matrix $\mathbf{H}$, as shown in Eq. 3.4. Similarly, the matrix of the sparsifying basis $\boldsymbol{\Psi}'$ is a smaller version of $\boldsymbol{\Psi}$ since the signal under analysis $\mathbf{F}_{mn}$ is a portion of

Table 3.1: **CASSI block reconstruction model variables**

Variable	Size	Description
$B \times B$		Dimensions of FPA windows
$N' = \frac{N}{B}$, $V' = \lceil \frac{N+L-1}{B} \rceil$		Number of windows
$\mathbf{F}_{mn} = \left[\mathbf{F}_{mn0}, \cdots, \mathbf{F}_{mn(L-1)}\right]$	$B \times B \times L$	$(m,n)^{th}$ oblique parallelepiped in the data cube
$\mathbf{f}_{mn} = \left[\mathbf{f}_{mn0}^T, \cdots, \mathbf{f}_{mn(L-1)}^T\right]^T$	B^2L	Vectorized form of $\mathbf{F}$
$\mathbf{Y}_{m,n}^i$	$B \times B$	$(m,n)^{th}$ CASSI measurement window in the i^{th} shot
$\mathbf{y}_{mn}^i$	B^2	Vectorized form of $\mathbf{Y}_{m,n}^i$
$\mathbf{y}_{mn} = \left[(\mathbf{y}_{mn}^0)^T, \cdots, (\mathbf{y}_{mn}^{K-1})^T\right]^T$	KB^2	Vectorized CASSI measurement window for K shots
$\mathbf{H}_{mn}^i$	$B^2 \times B^2L$	Block CASSI matrix for the i^{th} shot
$\mathbf{H}_{mn} = \left[\left(\mathbf{H}_{mn}^0\right)^T, \cdots, \left(\mathbf{H}_{mn}^{K-1}\right)^T\right]^T$	$KB^2 \times B^2L$	Block CASSI matrix for K shots

* In all equations equations $i = 0, \cdots, K-1$, $m = 0, \cdots, N'-1$, $n = V'-1$.

the data cube $\mathbf{F}$.

The full data cube $\hat{\mathbf{F}}$ is assembled by tiling the reconstructed oblique parallelepipeds. The relation between $\hat{\mathbf{F}}_{mn}$ and the complete reconstruction $\hat{\mathbf{F}}$ is the same as that in Eq. 3.3. Thus, the full data cube can be obtained by

$$\hat{\mathbf{F}}_k = \begin{bmatrix} \hat{\mathbf{F}}_{00k} & \cdots & \hat{\mathbf{F}}_{0(V'-1)k} \\ \vdots & \ddots & \vdots \\ \hat{\mathbf{F}}_{(N'-1)0k} & \cdots & \hat{\mathbf{F}}_{(N'-1)(V'-1)k} \end{bmatrix} \tag{3.7}$$

where $k = 0, \cdots, L-1$ indexes the spectral bands and $\hat{\mathbf{F}} = \left[\hat{\mathbf{F}}_0, \cdots, \hat{\mathbf{F}}_{L-1}\right]$.

In terms of reconstruction computational complexity, the number of operations per iteration in the GPSR algorithm depends on the underlying signal size and the size of the measurement vector. In particular, the GPSR in CASSI performs approximately $O(KN^4L)$ operations per iteration to recover a $N \times N \times L$ data cube using K FPA measurements. Similarly, recovering a $B \times B \times L$ oblique parallelepiped within the data cube requires $O(KB^4L)$ operations per iteration. Thus, the reconstructions from $(N')^2$ measurement blocks take $O\left(K\frac{N^4}{(N')^2}L\right)$ operations. Furthermore, the block reconstruction model can be distributed in multiple processor architectures. Assuming the number of cores is commensurate to the number of measurement windows, then the number of operations per core is $O\left(K\frac{N^4}{(N')^4}L\right)$. A summary of the variables of the CASSI block reconstruction model is presented in Table 3.1. A comparison between the features for the traditional and CASSI block reconstruction models is presented in Table 3.2.

Table 3.2: CASSI reconstruction models comparison

Feature	CASSI model	CASSI block model
Model in matrix notation	$\mathbf{y} = \mathbf{H}\mathbf{f} + \boldsymbol{\omega}$	$\mathbf{y}_{mn} = \mathbf{H}_{mn}\mathbf{f}_{mn} + \boldsymbol{\omega}_{mn}$
Spatial dimension of the data cube	N	$B \ll N$
Spectral dimension of the data cube	L	L
Number of CASSI shots	K	K
Number of non-zero elements in $\mathbf{H}$	KN^2L	KB^2L
Size of sensing matrix	$KN(N+L-1) \times N^2L$	$KB^2 \times B^2L$
Number of GPSR operations per iteration	$O(KN^4L)$	$O(KB^4L)$

Figure 3.3 shows the reconstruction of a spectral band using the block CASSI reconstruction model. There, it can be observed that assembling small parallelepiped data cubes recovered separately causes undesired block artifacts in the block boundaries. The next section addresses this issue by using vertical and horizontal overlapping pixels between measurement windows. This approach improves the quality of the reconstructions making the artifacts unnoticeable.

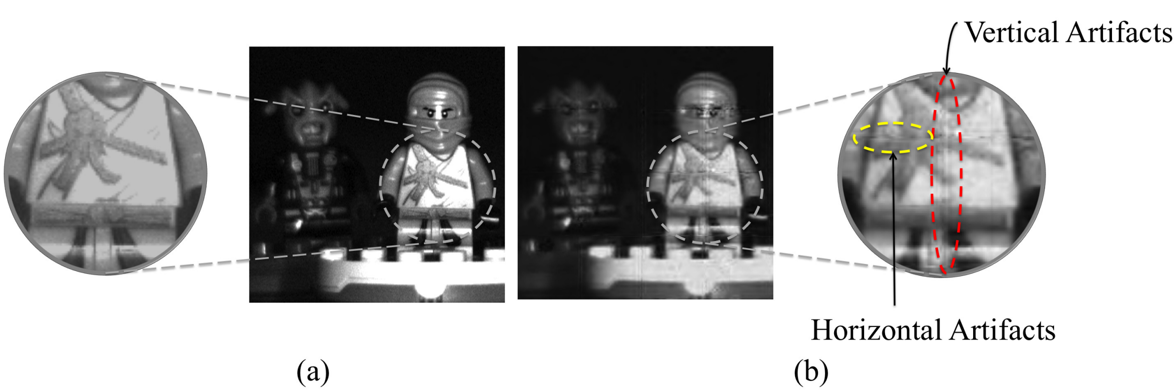

Figure 3.3: (a) Original spectral slice. (b) Reconstruction of a spectral band using the non-overlapping block-model of CASSI. Horizontal and vertical artifacts can be noticed on the block boundaries.

Chapter 4

LAPPED BLOCK RECONSTRUCTION MODEL

The lapped block model uses overlapped FPA windowed measurements. Then, a set of overlapped oblique parallelepipeds within the data cube is recovered. The full cube reconstruction process is described next.

4.1 Decomposition of the Measurement Set

Let Δ be the number of overlapping columns or rows between consecutive FPA measurement windows. Figure 4.1 shows an example of this approach in which two consecutive blocks horizontally and vertically share a set of ΔB elements. Lapped elements between windows cause that some entries of the matrix $\mathbf{H}$ affect more than one window. Equation 3.4 can then be rewritten for the block model with overlapping pixels by properly selecting the indices of rows and columns in the matrix $\mathbf{H}^i$ that affect a specific window. The $(\ell, j)^{th}$ element of the sub-matrix related to the $(m, n)^{th}$ window is given by

$$\left(\mathbf{H}^i_{mn}\right)_{\ell,j} = \left(\mathbf{H}^i\right)_{r'_\ell, r'_j} \tag{4.1}$$

with $r'_\ell = r_\ell - (m + nN) \cdot \Delta$ and $r'_j = r'_\ell + u \cdot (N^2 - N)$. The number of overlapping windows used is $N' \times V'$, where $N' = \lceil \frac{N}{B-\Delta} \rceil$ and $V' = \lceil \frac{N+L-1}{B-\Delta} \rceil$.

4.2 Data Cube Reconstruction from Lapped Measurement Windows

The use of lapped measurement windows leads to an overlap in the reconstructed set of parallelepipeds. Given the set of windowed measurements $\{\mathbf{y}_{mn}\}_{m=0,n=0}^{N'-1,V'-1}$, a compressed sensing reconstruction algorithm is used to recover $\{\tilde{\mathbf{f}}_{mn}\}_{m=0,n=0}^{N'-1,V'-1}$. This procedure is realized as described in Table 4.1.

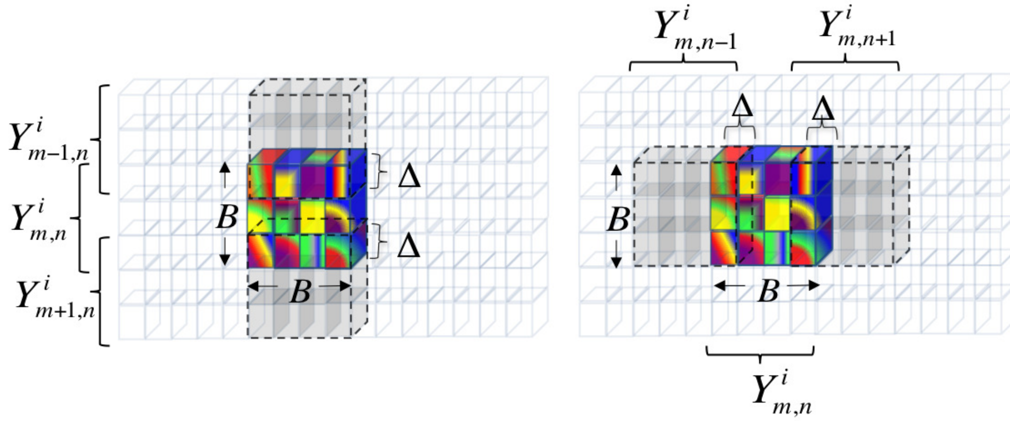

Figure 4.1: Example of the block-CASSI model using Δ overlapping rows and columns in the FPA measurement windows. Left: Horizontal overlapping, Right: Vertical overlapping.

Table 4.1: Individual block data cube reconstruction from Lapped Windows

Inputs	$\{\mathbf{Y}^i\}_{i=0}^{K-1}$, K, B, Δ
Initialization	$N' = \lceil \frac{N}{B-\Delta} \rceil$, $V' = \lceil \frac{N+L-1}{B-\Delta} \rceil$
Split measurement set	$\mathbf{Y}^i = \left[\mathbf{Y}^i_{0,0}, \cdots, \mathbf{Y}^i_{N'-1,V'-1}\right]$
Group blocks from different shots	$\mathbf{Y}_{m,n} = \left[\mathbf{Y}^0_{m,n}, \cdots, \mathbf{Y}^{K-1}_{m,n}\right]$
Vectorize measurements	$\mathbf{y}_{mn} = \left[\left(\mathbf{y}^0_{mn}\right)^T, \cdots, \left(\mathbf{y}^{K-1}_{mn}\right)^T\right]^T$
Use GPSR algorithm to recover individual oblique parallelepipeds within the data cube	$\tilde{\mathbf{f}}_{m,n} = \left[\left(\tilde{\mathbf{f}}_{0,0}\right)^T, \cdots, \left(\tilde{\mathbf{f}}_{N'-1,V'-1}\right)^T\right]^T$
Rearrange the results	$\tilde{\mathbf{F}}_{m,n} = \left[\tilde{\mathbf{F}}_{0,0}, \cdots, \tilde{\mathbf{F}}_{N'-1,V'-1}\right]$

Once the individual parallelepipeds are obtained, these are merged to assemble the full data cube. The merging process is critical since this will help in reducing the block reconstruction artifacts, improving the quality of the reconstructions.

Let $\tilde{\mathbf{F}}_{m,n}$ be the matrix representation of the recovered oblique parallelepiped within the data cube obtained from the inverse of $\mathbf{y}_{mn}$. The relation between overlapped measurement windows, and the recovered lapped oblique parallelepipeds within the data cube is depicted in Fig. 4.2.

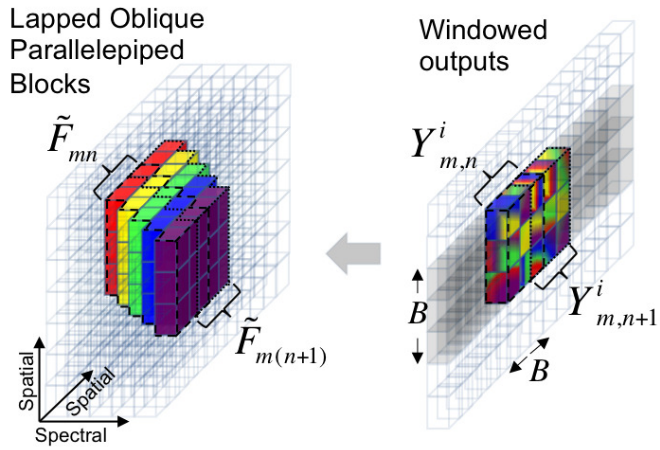

Figure 4.2: Vertically overlapped measurement windows lead to vertically overlapped oblique parallelepipeds within the data cube. Horizontally overlapped measurement windows and their reconstructions have a similar relation.

Each spectral band of the recovered portion can be expressed as

$$\tilde{\mathbf{F}}_{m,n,k} = \begin{bmatrix} & \mathcal{A}_{m,n,k} & \\ \mathcal{C}_{m,n,k} & \mathcal{B}_{m,n,k} & \mathcal{D}_{m,n,k} \\ & \mathcal{E}_{m,n,k} & \end{bmatrix} \tag{4.2}$$

where $\mathcal{A}_{mnk}$, $\mathcal{C}_{mnk}, \mathcal{D}_{mnk}$ and $\mathcal{E}_{mnk}$ are regions recovered from adjacent measurement windows. More specifically, $\mathcal{A}_{mnk}$ is also obtained from $\tilde{\mathbf{F}}_{m-1,n}$, $\mathcal{C}_{mnk}$ is also contained in $\tilde{\mathbf{F}}_{m,n-1}$, and so on. In contrast, $\mathcal{B}_{mnk}$ is the portion of the window that did not use overlapped pixels for the recovery; therefore, it is contained only in $\tilde{\mathbf{F}}_{m,n}$. Figure 4.3 presents a general description for the overlapped structure in Eq. 4.2. This methodology is also well suited for the special cases occurred in the image boundaries as depicted.

The merging process is realized such that duplicated regions of consecutive blocks are averaged and assembled with the set $\{\mathcal{B}_{m,n,k}\}_{m=0,n=0}^{N'-1,V'-1}$ as shown in Fig. 4.4. Other approaches such as median or myriad filters [25, 22] are also valid alternatives for reducing blocking artifacts and can be explored in future work. Let the average between overlapped regions of consecutive blocks be defined as

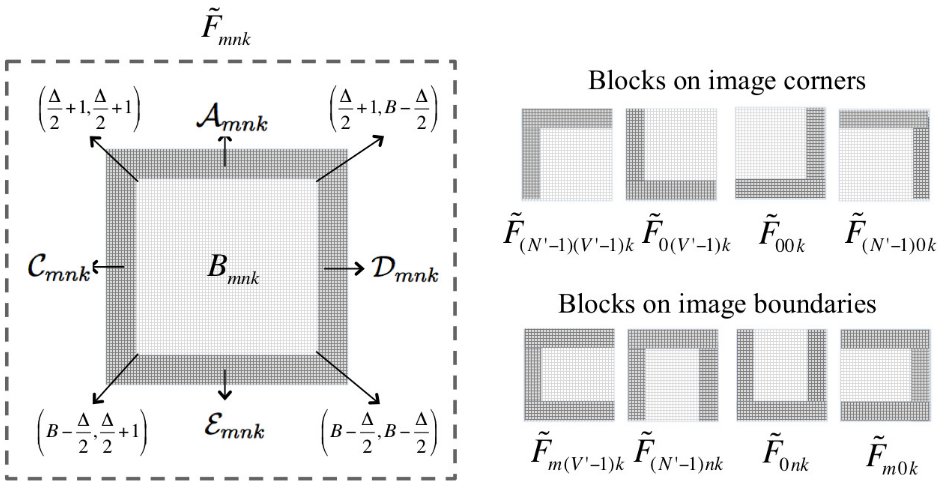

Figure 4.3: Left: Subdivision of the k^{th} spectral band of a recovered block of the data cube. Shaded regions correspond to $\frac{\Delta}{2}$ columns or rows on each side. Pixels in those regions are duplicated since they are reconstructed by the $(m,n)^{th}$ block and one of its four neighbors. Right: Special cases for the blocks in the boundaries of the image.

$$\mathcal{E}'_{m(m+1),n,k} = \frac{\mathcal{E}_{m,n,k} + \mathcal{A}_{(m+1),n,k}}{2} \quad , \quad \mathcal{D}'_{m,n(n+1),k} = \frac{\mathcal{D}_{m,n,k} + \mathcal{C}_{m,(n+1),k}}{2} \tag{4.3}$$

for $m = 0, \cdots, N'-1$ and $n = 0, \cdots, V'-1$. From Fig. 4.4, it can be seen that the portion of each oblique parallelepiped for the merging process is given by

$$\hat{\mathbf{F}}_{m,n,k} = \begin{bmatrix} \mathcal{B}_{m,n,k} & \mathcal{D}'_{m,n(n+1),k} \\ & \mathcal{E}'_{m(m+1),n,k} \end{bmatrix}. \tag{4.4}$$

Finally, the k^{th} spectral band $\hat{\mathbf{F}}_k$ of the complete data cube can be assembled as

$$\hat{\mathbf{F}}_k = \begin{bmatrix} \hat{\mathbf{F}}_{0,0,k} & \hat{\mathbf{F}}_{0,1,k} & \cdots & \hat{\mathbf{F}}_{0,V'-1,k} \\ \vdots & \vdots & \ddots & \vdots \\ \hat{\mathbf{F}}_{N'-1,0,k} & \hat{\mathbf{F}}_{N'-1,1,k} & \cdots & \hat{\mathbf{F}}_{N'-1,V'-1,k} \end{bmatrix} \tag{4.5}$$

for $k = 1, \cdots, L$ and the complete reconstruction is given by $\hat{\mathbf{F}} = \left[\hat{\mathbf{F}}_0, \cdots, \hat{\mathbf{F}}_{L-1}\right]$.

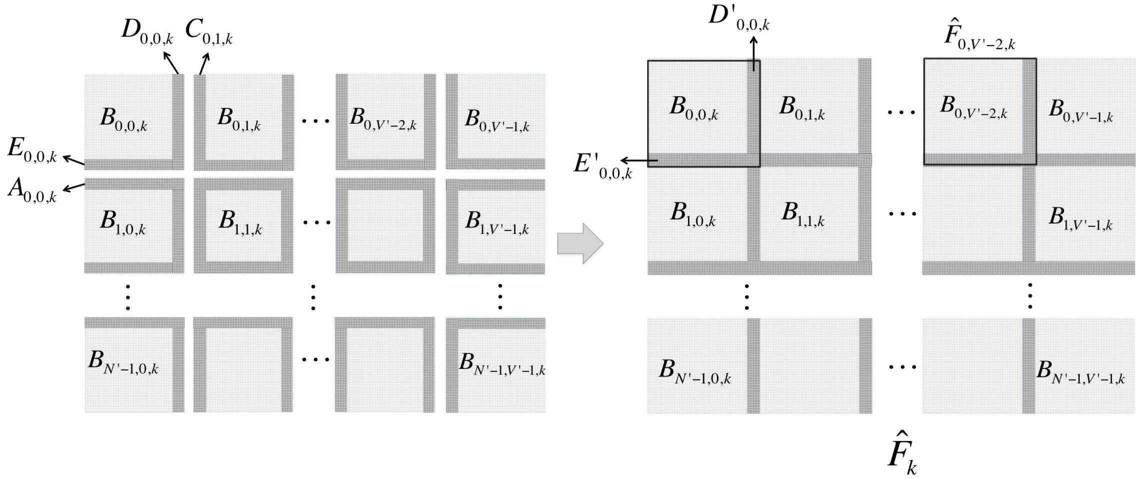

Figure 4.4: Tiling in the reconstruction of a spectral band. The shaded zones show the average of the overlapped regions on consecutive parallelepipeds.

The data cube merging process is summarized in Table 4.2. The block size and number

Table 4.2: Summary: Merging process for Lapped Block CASSI model

Inputs: $\{\tilde{\mathbf{F}}_{m,n,k}\}_{m=0,n=0,k=0}^{N'-1,V'-1,L-1}, N', V', L$

for $k = 0, \cdots, L-1$
  for $m = 0, \cdots, N'-1$
    for $n = 0, \cdots, V'-1$
      Extract $\mathcal{B}_{m,n,k}$ from $\tilde{\mathbf{F}}_{m,n,k}$
      Average the duplicated regions: $\mathcal{E}'_{m(m+1),n,k}$ *and* $\mathcal{D}'_{m,n(n+1),k}$
      Use the template for assembling $\hat{\mathbf{F}}_{m,n,k} = \begin{bmatrix} \mathcal{B}_{m,n,k} & \mathcal{D}'_{m,n(n+1),k} \\ & \mathcal{E}'_{m(m+1),n,k} \end{bmatrix}$
    end
  end
  Assemble the k^{th} spectral band $\hat{\mathbf{F}}_k = \begin{bmatrix} \hat{\mathbf{F}}_{0,0,k} & \cdots & \hat{\mathbf{F}}_{0,V'-1,k} \\ \vdots & \ddots & \vdots \\ \hat{\mathbf{F}}_{N'-1,0,k} & \cdots & \hat{\mathbf{F}}_{N'-1,V'-1,k} \end{bmatrix}$
end

Output: $\tilde{\mathbf{F}} = \left[\tilde{\mathbf{F}}_0, \cdots, \tilde{\mathbf{F}}_{L-1}\right]$

of overlapping pixels determine the total number of blocks and thus, the amount of reconstructions needed to obtain the whole 3D scene. The selection of these parameters gives a trade-off in terms of the quality of the reconstructed images and the time that it takes to recover each parallelepiped.

Chapter 5

SIMULATION RESULTS

Simulations were conducted to test the performance of the lapped block reconstructions using CASSI measurements. Three test data cubes $\mathbf{F}$ with spatial resolution of 256×256, 512×512 and 1024×1024 pixels and $L = 24$ spectral bands in the range of 452nm to 667nm were used. The 256×256 test data cube and its center frequencies are shown in Fig. 5.1. The 512×512 and 1024×1024 data cubes are shown in Fig. 5.2 and Fig. 5.3, respectively. A fourth data cube with spatial resolution of 512×512 pixels and $L = 32$ spectral bands was used to analyze the lapped block reconstruction approach for an increase in the spectral resolution. This database is a portion of the Moffett field aerial view captured by AVIRIS[1], ranging from 447nm to 737nm. An RGB representation of this database is presented in Fig. 5.8 (a). In all the experiments, the sensing process is simulated using random boolean coded apertures $T^i_{j\ell} \in \{0, 1\}$ with transmittance of 50% pixels. Then, compressed sensing reconstructions were obtained using the GPSR algorithm [14] with the lapped block reconstruction model procedures in Tables 4.1 and 4.2. These results are compared with the traditional full data cube recovery from the CASSI model in Chapter 2. Both approaches used the same number of iterations. However, it is observed that the lapped block reconstruction converges faster. The regularization parameter for the GPSR algorithm was selected such that each simulation uses the value that results in the best reconstruction. In the lapped block reconstructions, the same value of τ was used for recovering all the blocks. A 3D representation basis $\mathbf{\Psi} = \mathbf{\Psi}_C \otimes \mathbf{\Psi}_{2D}$ was used, where $\mathbf{\Psi}_C$ is the Cosine basis and $\mathbf{\Psi}_{2D}$ is a 2D Wavelet Symmlet 8 basis. Using the 3D representation basis, only the 3% of the coefficients are needed to preserve the 99.64% of the signal's energy. Each data cube was approximated using a sparsity ratio $S/v = 0.065$, where $v = N^2L$, by setting to zero the $v - S$ least significant coefficients of its sparse representation and using this data cube as the signal under analysis. For this approximation, the data cubes $\mathbf{F}$ are represented as a v-long vector using Eq. 2.3. The block size in all the experiments must be a dyadic value, such that the Wavelet representation of the signal can be computed. All simulations were conducted and timed using an Intel Core i7 3960X 3.30GHz processor, and 32 GB RAM memory.

5.1 Lapped Block Reconstructions

In this experiment, the test data cubes are recovered using different block-sizes and amount of overlap between measurement blocks. The parameters used in this simulations for each data cube are presented in Table 5.1.

Table 5.1: Parameters for lapped block reconstructions

Data cube	Block-size B	Overlap Δ
256×256	32	12
	64	24
512×512	64	24
	128	30
1024×1024	128	32
	256	40

Figure 5.4 shows the results for PSNR as a function of the number of FPA measurements for the lapped block CASSI model and the traditional full data cube reconstruction. Figures 5.4 (a) and (b), show that the lapped block reconstruction outperforms the results of the traditional CASSI reconstruction for the 256×256 and 512×512 data cubes. The results for the 1024×1024 data cube are slightly different as the new approach points to better PSNR when more than 6 shots were used. However, the use of smaller block-sizes for this data cube can lead to PSNR improvements such as those in Fig. 5.4 (a) and (b). Notice that the results for the traditional CASSI reconstructions using more than 12 shots in Fig. 5.4 (c) are not shown. For these cases, the computational burden is such that the workstation used for the simulations was

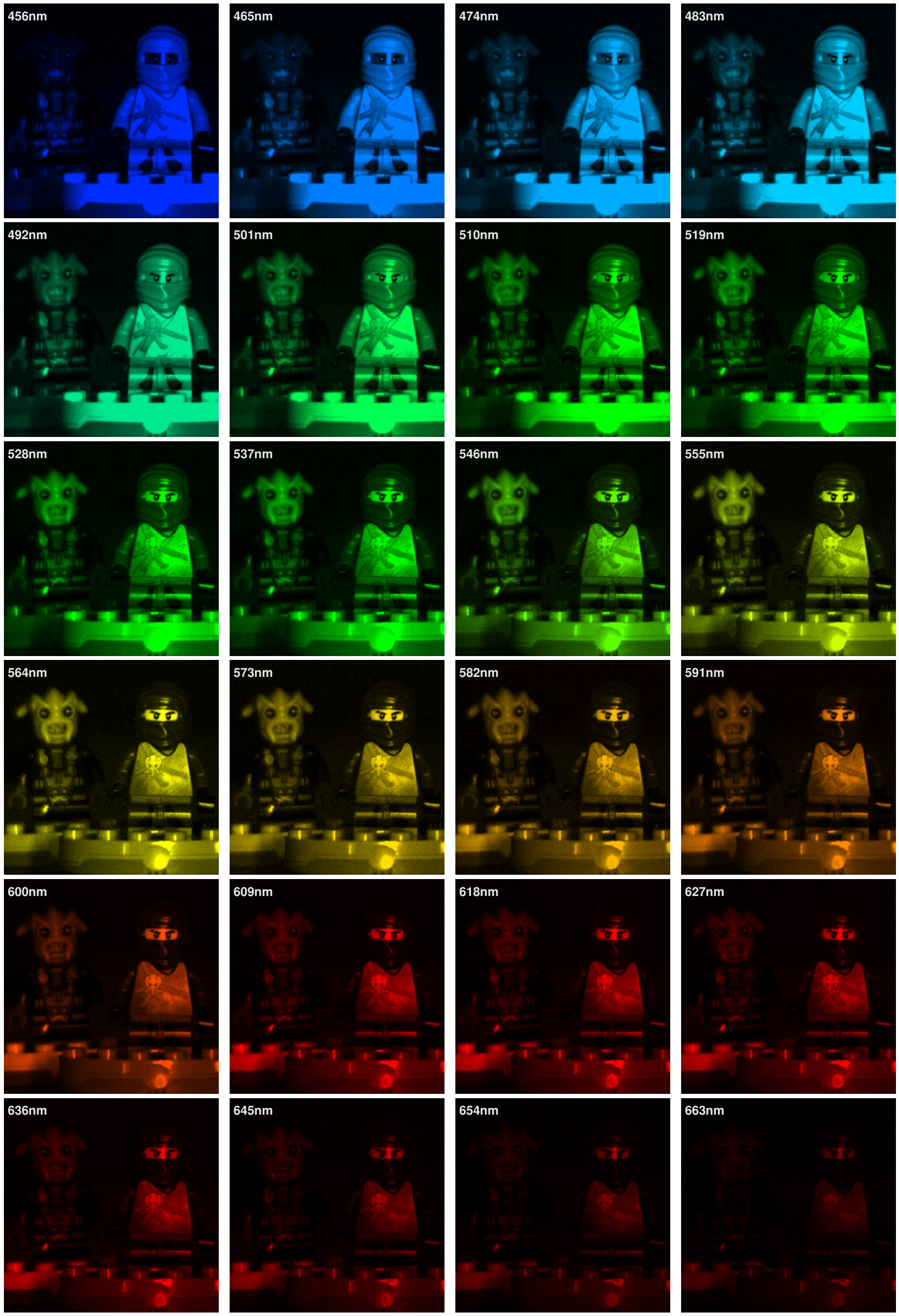

Figure 5.1: 24 spectral band data cube with wavelengths ranging from 452nm to 667nm. Each spectral slice has a spatial resolution of 256×256 pixels.

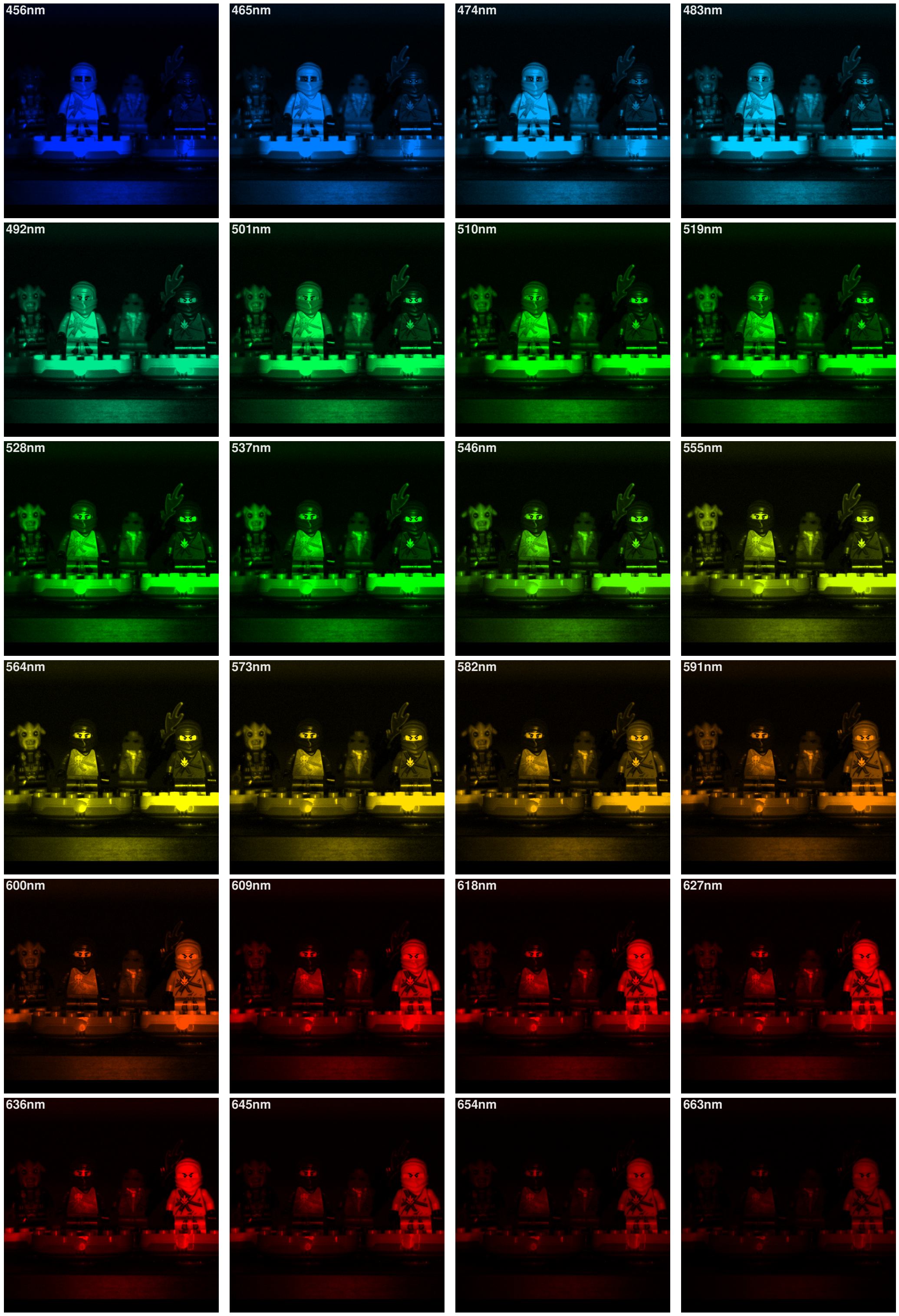

Figure 5.2: 24 spectral band data cube with wavelengths ranging from 452nm to 667nm. Each spectral slice has a spatial resolution of 512×512 pixels.

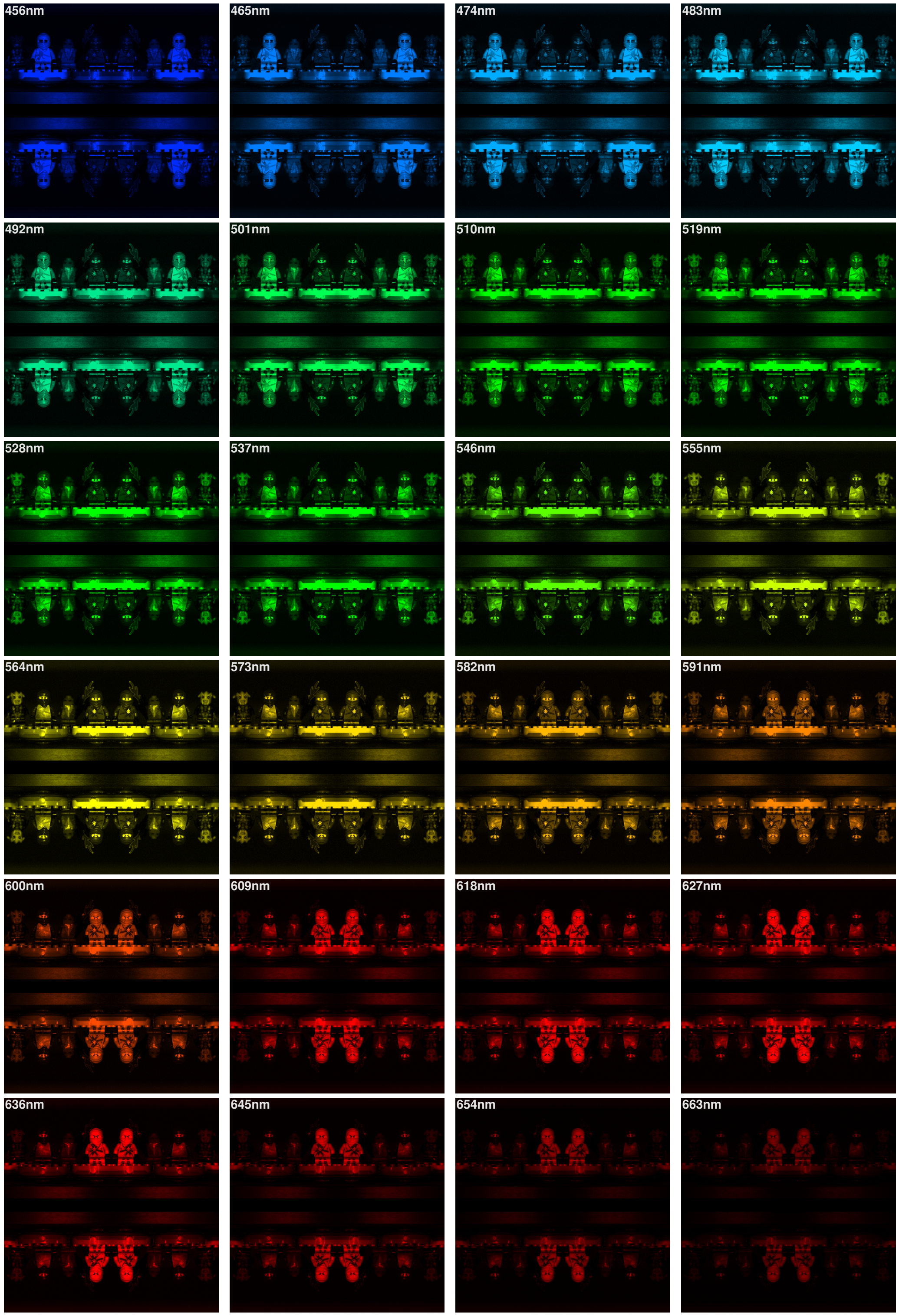

Figure 5.3: 24 spectral band data cube with wavelengths ranging from 452nm to 667nm. Each spectral slice has a spatial resolution of 1024×1024 pixels.

not capable to obtain the reconstructions. Many commercial hardware architectures are capable to recover small data cubes, but solving the problem for larger spatial resolutions is time and computationally demanding such that these reconstructions are not attainable. The lapped block reconstruction approach provides the framework to solve these problems. Similar results were obtained for the $512 \times 512 \times 32$ data cube as shown in Fig. 5.4 (d).

In general, simulations show that the lapped block reconstructions result in an improvement of up to 5 dB over the traditional reconstruction approach. Figure 5.5 illustrates a comparison of the reconstructed quality of the $256 \times 256 \times 24$ data cube. Zoomed versions of the results for the $512 \times 512 \times 24$ and $1024 \times 1024 \times 24$ data cubes using $B = 64$, $\Delta = 24$ and $B = 128$, $\Delta = 24$, are shown in Fig. 5.6 and 5.7, respectively. Reconstructions for the aerial view of Moffet field are shown in Fig. 5.8. In addition, the spectral reconstruction for three pixels from Fig. 5.5 is presented in Fig. 5.9. It can be noticed that the lapped block reconstruction provides a more accurate approximation of the spectral information of the source than the complete reconstruction.

5.2 Lapped Block Reconstructions from Noisy Measurements

Reconstructions from noisy measurements were obtained for both, traditional approach and the lapped block reconstruction method. In this experiment, zero-mean Gaussian noise was added to the set of FPA measurements $\mathbf{y}$ in Eq. 2.6. The variance of the noise was selected such that a desired signal to noise ratio (SNR) was achieved. The SNR can be expressed as $\text{SNR} = 10 \log_{10}\left(\frac{\sigma_y^2}{\sigma_n^2}\right)$, where σ_y^2 is the variance of the FPA measurement set $\mathbf{y}$, and σ_n^2 is the variance of the noise.

Simulation results for 20 dB and 25 dB of SNR using the $256 \times 256 \times 24$ database are presented in Fig. 5.10. These results show that despite of the presence of those levels of noise in the measurement set, the lapped block reconstruction approach overcomes the results of the full data cube reconstruction.

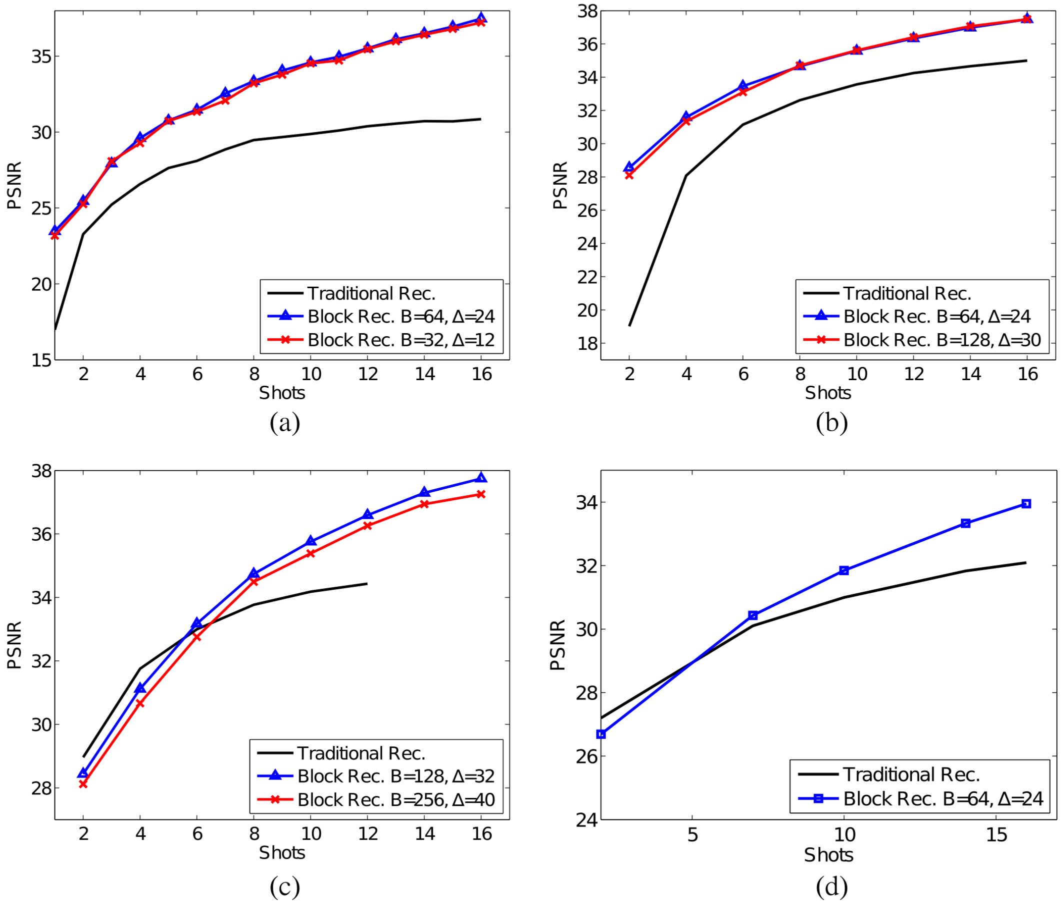

Figure 5.4: Reconstruction (Rec.) PSNR for the full data cube reconstruction and by the lapped block CASSI reconstruction for the (a) $256 \times 256 \times 24$, (b) $512 \times 512 \times 24$, (c) $1024 \times 1024 \times 24$, and (d) $512 \times 512 \times 32$ data cubes.

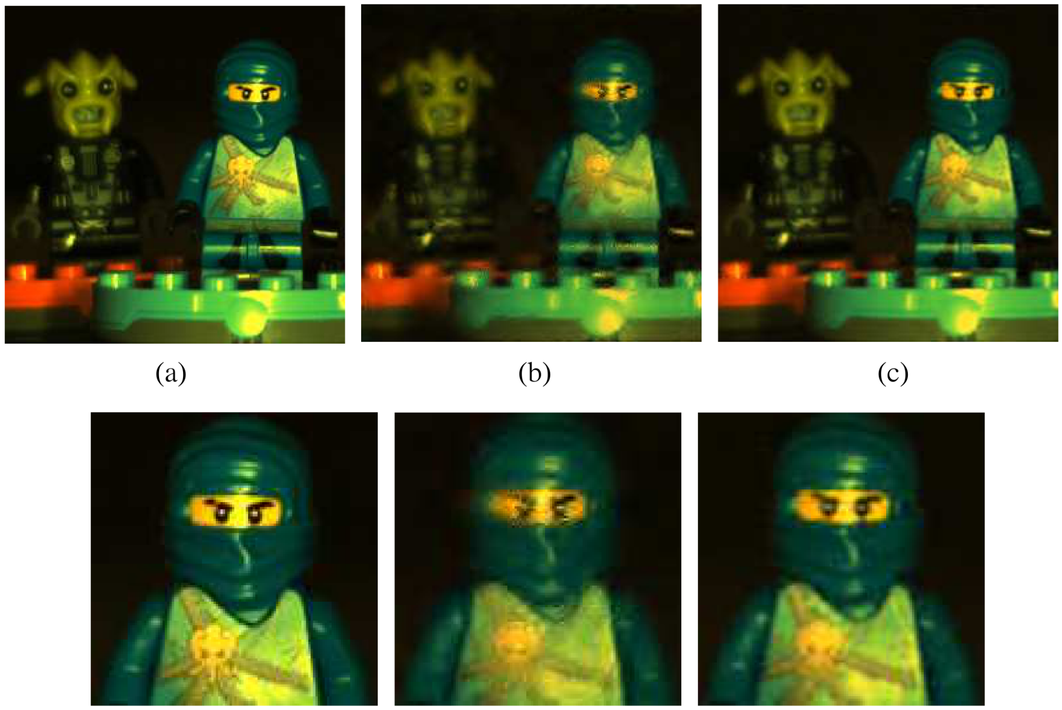

(a) (b) (c)

(c) (d) (e)

Figure 5.5: (a) Original $256 \times 256 \times 24$ data cube. Reconstructions for 6 FPA measurement shots using: (b) Traditional reconstruction approach, 28.1 dB; (c) Lapped block approach with block size $B = 64$ and overlap $\Delta = 24$, 31.46 dB. (d), (e) and (f) are zoomed versions of (a), (b) and (c), respectively.

5.3 Time for Reconstruction

Since block reconstructions manipulate smaller matrices, the reconstruction time needed for each block in Eq. 4.2 is much lower than that of the traditional approach. However, the block size provides a trade-off between the time required for reconstruction and the quality of the reconstructed images. The selection of the block size depends both on the spatial and spectral dimensions of the data cube since smaller blocks may not contain enough information across all spectral bands to provide accurate reconstructions. Moreover, the use of smaller block sizes clearly leads to a larger number of blocks to recover, in consequence, more processors are required in order to accelerate the reconstruction. Also, smaller block sizes degrade the image quality. On the other hand, the use of larger block sizes increases the reconstruction time of an

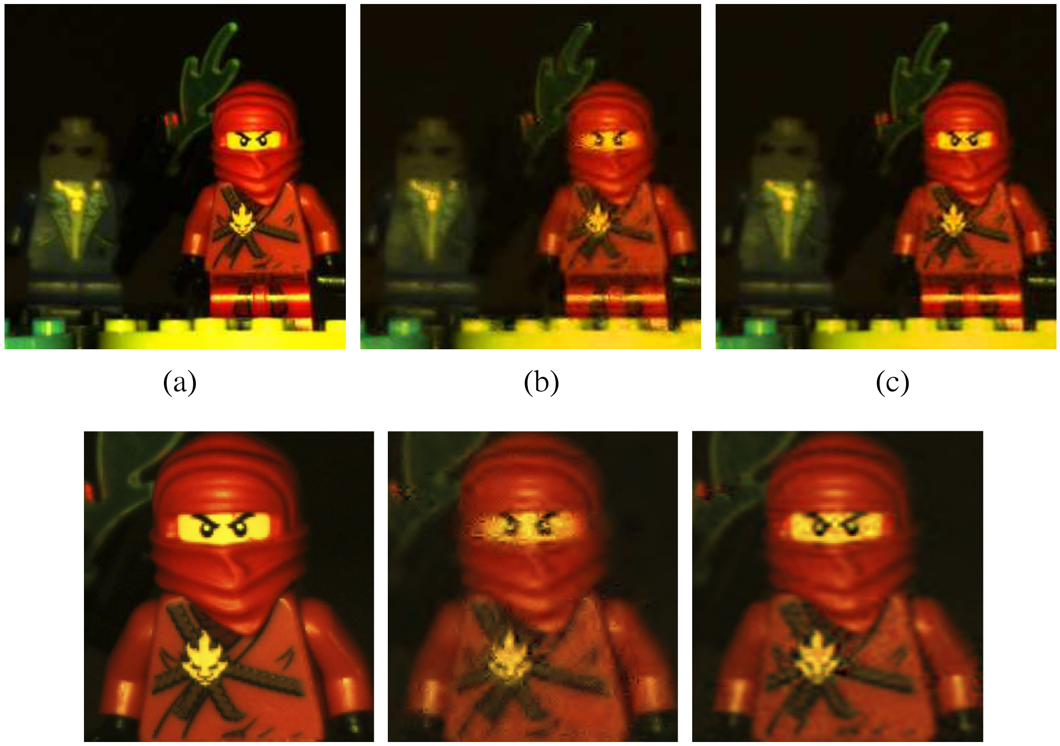

(a) (b) (c)

(d) (e) (f)

Figure 5.6: (a) Original zoomed versions of the $512 \times 512 \times 24$ data cube. Reconstructions for 6 FPA measurements using: (b) Traditional reconstruction, 31.09 dB; (c) Lapped block reconstruction with block size $B = 64$ and overlap $\Delta = 24$, 33.45 dB. (d),(e), and (f) are zoomed versions of (a), (b), and (c), respectively.

individual block but could lead to a reduction in the time for recovering all the blocks depending on the number of processors available.

Figure 5.11 presents the reconstruction time for the experiments conducted in Section 5.1. It can be noticed that block recovery is up to 4 times faster than recovering the $256 \times 256 \times 24$ data cube at once, and up to 5 times for the $512 \times 512 \times 24$ data cube. For larger spatial dimensions, such as $1024 \times 1024 \times 24$, the blocked approach is up to 9 times faster, and for a large number of FPA measurements, the reconstructions can take several days for the traditional approach. These simulation results also show that increasing the spectral resolution leads to an increase of the reconstruction time with respect to a data cube with the same spatial dimensions. However, the lapped block

(a) (b) (c)

Figure 5.7: (a) Original zoomed version of the $1024 \times 1024 \times 24$ data cube. Reconstructions for 6 FPA measurements using: (b) Traditional reconstruction, 32.99 dB, and (c) Lapped block reconstruction with $B = 128$ and $\Delta = 32$, 33.17 dB.

(a) (b) (c)

Figure 5.8: (a) Original RGB and zoomed version of the $512 \times 512 \times 32$ data cube. Reconstructions for 10 FPA measurement shots using: (b) Traditional reconstruction approach, 30.99 db, and (c) Lapped block approach with block size $B = 64$ and overlap $\Delta = 24$, 31.84 dB.

reconstruction approach is still faster than the complete reconstruction. In addition, Fig. 5.11 shows the average time to recover only one block using a single processor. This can be used for designing multi-processor and parallel schemes to recover the less number of blocks per processor and thus, reduce the reconstruction time for specific applications.

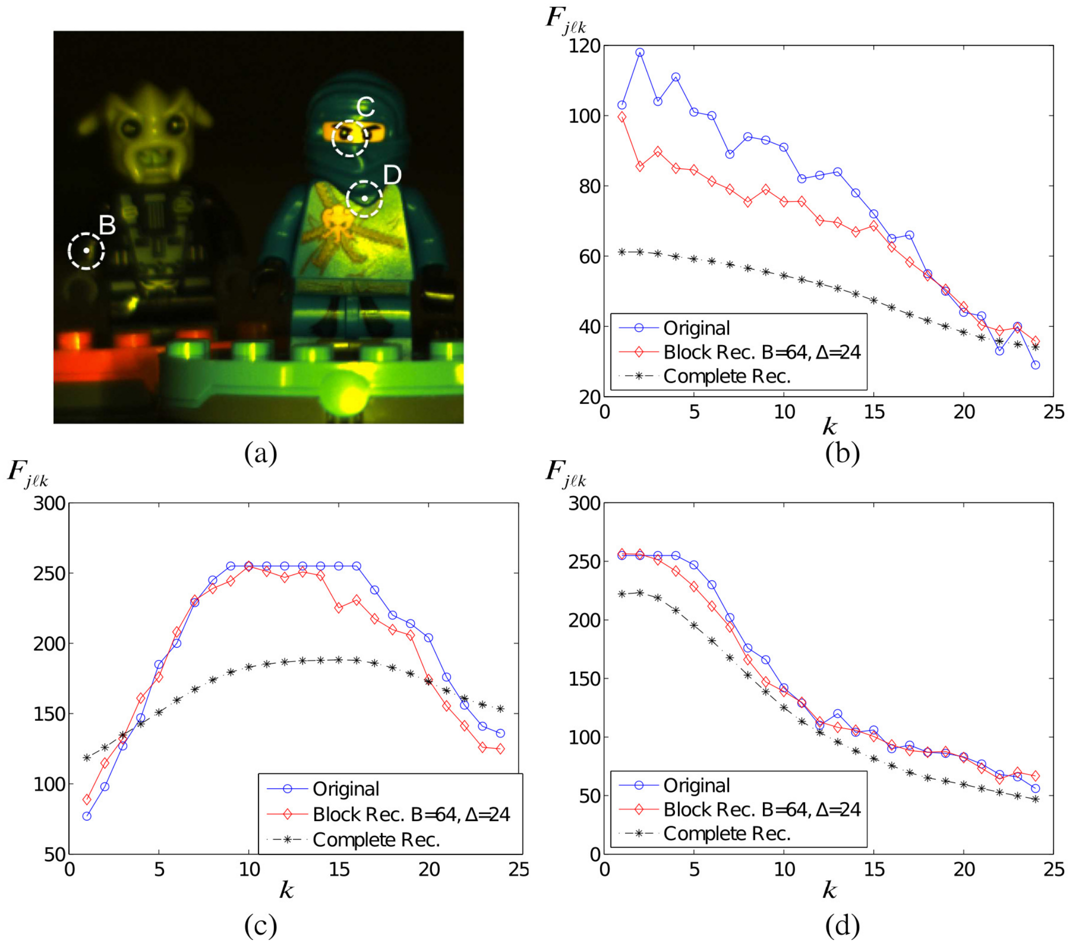

Figure 5.9: Spectral reconstruction of the highlighted pixels in (a) for (b) pixel B, (c) pixel C, and (d) pixel D.

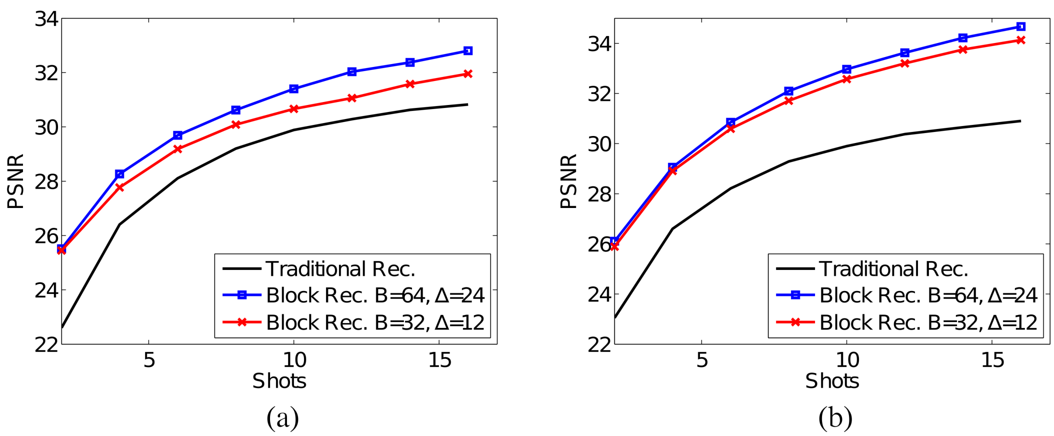

Figure 5.10: Reconstruction (Rec.) PSNR from noisy measurements, for the $256 \times 256 \times 24$ full data cube reconstruction and by the lapped block reconstruction. (a) SNR $=$ 20 dB and (b) SNR $=$ 25 dB.

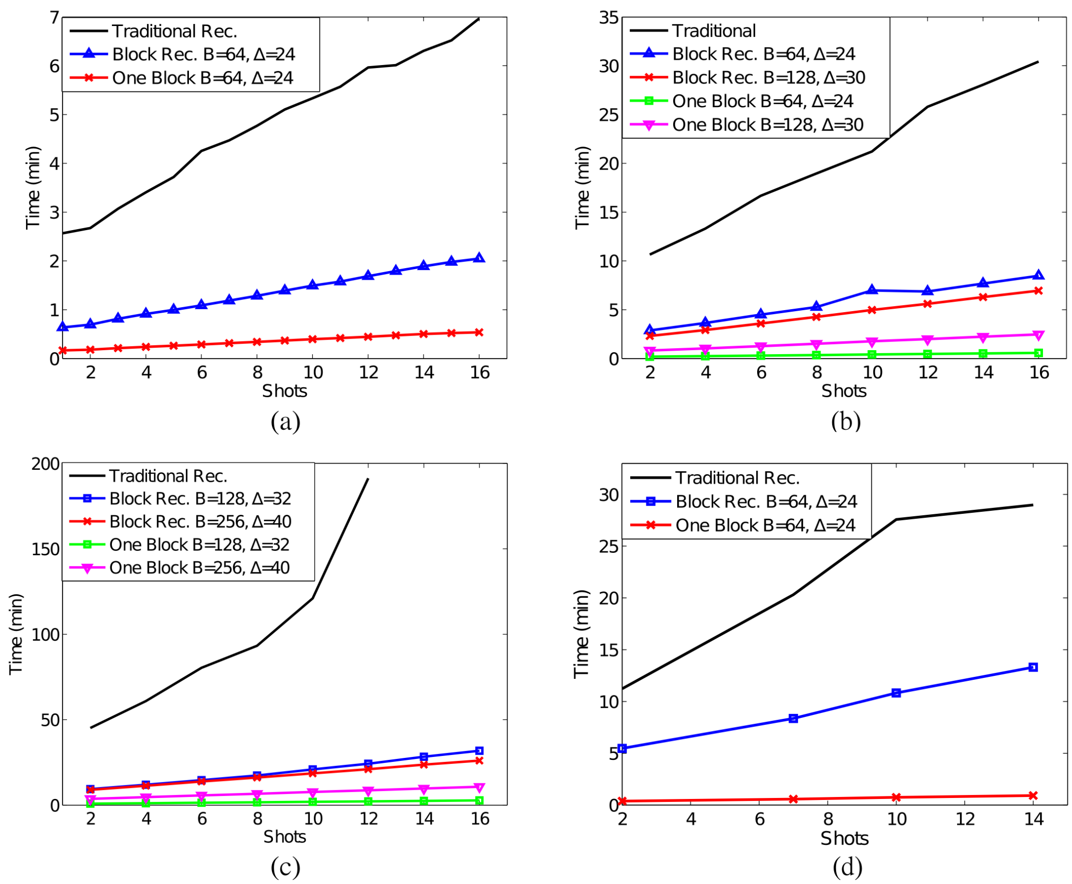

Figure 5.11: Reconstruction (Rec.) time as a function of the number of FPA measurements. Results for the traditional reconstruction and lapped block reconstruction approaches are shown. The average time for recovering an individual block using a single processor (One block) is also presented for (a) 256×256, (b) 512×512 and, (c) 1024×1024 spatial dimensions of the data cubes with $L = 24$ spectral bands and (d) $512 \times 512 \times 32$ data cube.

Chapter 6

CONCLUSIONS

The mathematical model for block reconstructions in CASSI system has been developed. The structure of the compressed measurements in CASSI is suitable for recovering independent oblique parallelepipeds within the underlying data cube. Two variations of the block reconstruction model were described: the first one uses non-overlapping windows in the mesurement set and the second uses lapped windows. Blocking artifacts can appear in the reconstructions when non-overlapping measurement windows are used. However, the artifacts are significantly reduced when lapped measurement windows are used. A merging process for lapped windows was proposed. This process is based on averages but other alternatives such as median filters can be used.

The proposed block reconstruction method is well suited for multi-processor architectures in which each block is recovered by a single processor. The computational cost of recovering a data cube from $(N')^2 = \lfloor \frac{N}{B} \rfloor^2$ measurement windows is reduced by a factor of $(N')^2$ per iteration of the GPSR, since the complexity of the block reconstruction approach has complexity $O\left(K \frac{N^4}{(N')^2} L\right)$ instead of the $O(KN^4L)$ complexity of the traditional reconstruction model. Also, simulations for different variations of the spatial and spectral dimensions of the data cube, block size, number of overlapping pixels and presence of noise in the measurement set, show that the proposed model leads to a reduction of the reconstruction time and improvements of the image quality. In particular, the lapped reconstructions result in an improvement of up to 5 dB over the traditional approach, and the reconstruction time is reduced up to an order of magnitude.

The results of this work have been recently published in [5].

6.1 Future Work

This work does not include and analysis for spectral images in which the number of bands exceeds the spatial resolution. Additional work, taking into account the block size, is required for this type of signals since the windows in the boundaries of the FPA measurement might not contain enough information to obtain a good reconstruction of the corresponding parallelepiped.

A more precise discretization model for CASSI system has been recently published in [6]. The development of a lapped reconstruction model for the higher-order CASSI is an interesting area to continue this work.

BIBLIOGRAPHY

[1] Airborne visible infrared imaging spectrometer. http://aviris.jpl.nasa.gov/data/free_data.html.

[2] H. Arguello and G. Arce. Rank minimization code aperture design for spectrally selective compressive imaging. *IEEE Transactions on Image Processing*, 22(3):941 – 954, 2013.

[3] H. Arguello and G. R. Arce. Code aperture optimization for spectrally agile compressive imaging. *J. Opt. Soc. Am. A*, 28(11):2400–2413, 2011.

[4] H. Arguello and G. R. Arce. Spectrally selective compressive imaging by matrix system analysis. *OSA Optics and Photonics Congress, Monterey, CA.*, June 2012.

[5] H. Arguello, C. V. Correa, and G. R. Arce. Fast lapped reconstructions in compressive spectral imaging. *Applied Optics*, 52(10):D32 – D45, 2013.

[6] H. Arguello, H. Rueda, Y. Wu, D. W. Prather, and G. R. Arce. Higher-order computational model for coded aperture spectral imaging. *Applied Optics*, 52(10):D12 – D21, 2013.

[7] J. Bioucas-Dias and M. Figueiredo. A new twist: Two-step iterative shrinking/thresholding algorithms for image restoration. *IEEE Transactions on Image Processing*, 16(12):2992–3004, 2007.

[8] D. Brady and M. Gehm. Compressive imaging spectrometers using coded apertures. *Proc. of SPIE Vol.*, 6246:62460A–1.

[9] R. Chartrand. Exact reconstruction of sparse signals via nonconvex minimization. *IEEE Signal Processing Letters*, pages 707–710, 2007.

[10] Brandon M. Davis, Amanda J. Hemphill, Derya Cebeci Maltas, Michael A. Zipper, Ping Wang, and Dor Ben-Amotz. Multivariate hyperespectral raman imaging using compressive detection. *Analitical Chemistry*, 83(13):5986 – 5092, 2011.

[11] D. Donoho, Y. Tsaig, I. Drori, and J. Starck. Sparse solution of uderdetermined linear equations by stagewise orthogonal matching pursuit (stomp). *Stanford Univ., Palo Alto, CA, Stat. Dept. Tech. Rep.*, 26(3):301–321, March 2006.

[12] M. F. Duarte and R. G. Baraniuk. Kronecker compressive sensing. *IEEE Trans. on Image Processing*, 21(2):494–504, 2012.

[13] Y. Fang, L. Chen, J. Wu, and B. Huang. Gpu implementation of orthogonal matching pursuit for compressive sensing. *IEEE 17th International Conference on Parallel and Distributed Systems (ICPADS)*, pages 1044 –1047, 2011.

[14] M. Figueiredo, R. Nowak, and S. Wright. Gradient projection for sparse reconstruction: Application to compressed sensing and other inverse problems. *IEEE J. of Selected Topics in Signal Processing*, 1(4):586–597, 2007.

[15] C. Fisher and I. Kakoulli. Multispectral and hyperspectral imaging technologies in conservation: current research and potential applications. *Reviews in conservation*, (7), 2006.

[16] L. Gan. Block compressed sensing of natural images. *Proc. Int. Conf. Dig. Signal Process., Cardiff, U.K.*, pages 403–406, July 2007.

[17] Y. Garini, I. T. Young, and G. McNamara. Spectral imaging: principles and applications. *Cytometry Part A*, 69(8):735–747, 2006.

[18] M. Gehm and D. Brady. High-throughput hyperspectral microscopy. *Proc. of SPIE*, 6090, 2006.

[19] M. Gehm, M. Kim, C. Fernandez, and D. Brady. High-throughput, multiplexed pushbroom hyperspectral microscopy. *Optics Express*, 16(15):11032–11043, 2008.

[20] M. Green, R. Eastwood, C. Sarture, T. Chrien, M. Aronsson, B. Chippendale, J. Faust, B. Pavri, C. Chovit, and M. Solis. Imaging spectroscopy and the airborne visible/infrared imaging spectrometer (aviris). *Remote Sensing of Environment*, 65(3):227–248, 1998.

[21] A. Jurado-Lpez and M. Luque. Use of near infrared spectroscopy in a study of binding media used in paintings. *Analytical and Bioanalytical Chemistry*, 380(4):706 – 711, 2004.

[22] S. Kalluri and G. R. Arce. Robust frequency-selective filtering using weighted myriad filters admitting real-valued weights. *IEEE Transactions on Signal Processing*, 49(11):2721 –2733, 2001.

[23] D. Kittle, K. Choi, A. A. Wagadarikar, and D. J. Brady. Multiframe image estimation for coded aperture snapshot spectral imagers. *Appl. Opt.*, 49(36):6824–6833, 2010.

[24] D. Lau, C. Villis, S. Furman, and M. Livett. Multispectral and hyperspectral image analysis of elemental and micro-raman maps of cross-sections from a 16th century painting. *Analytica chimica acta*, 610(1):15 – 24, 2008.

[25] M. P. McLoughlin and G. R. Arce. Deterministic properties of the recursive separable median filter. *IEEE Transactions on Acoustics Speech and Signal Processing*, 35(1):98 –106, 1987.

[26] D. Needell and J. Tropp. Iterative signal recovery from incomplete and inaccurate samples. *Applied and Computational Harmonic Analysis*, 26(3):301–321, 2009.

[27] Y. Rivensons and A. Stern. Compressed imaging with a separable sensing operator. *IEEE Signal Process. Lett.*, 16(6):449–452, 2009.

[28] G. Shaw and H. Burke. Spectral imaging for remote sensing. *Lincoln Laboratory Journal*, 14(1):3–28, 2003.

[29] J. Shihao, X. Ya, and L. Carin. Bayesian compressive sensing. *IEEE Transactions Signal Processing*, 56(6):2346–2356, 2008.

[30] W. Smith, D. Zhou, and F. Harrison. Hyperspectral remote sensing of atmospheric profiles from satellites and aircraft. *Proc. of SPIE 4151, Hyperspectral Remote Sensing of the Land and Atmosphere*, pages 94–102, 2001.

[31] J. Tropp and A. Gilbert. Signal recovery from random measurements via orthogonal matching pursuit. *IEEE Transactions on Information Theory*, 53(12):4655–4666, 2007.

[32] J. Tropp and S. Wright. Computational methods for sparse solution of linear inverse problems. *Proceedings of the IEEE*, 98(6):948–958, 2010.

[33] A. Wagadarikar, R. John, R. Willett, and D. Brady. Single disperser design for coded aperture snapshot spectral imaging. *Appl. Opt.*, 47:B44–B51, 2008.

[34] A. Wagadarikar, N. Pitsianis, X. Sun, and D. Brady. Video rate spectral imaging using a coded aperture snapshot spectral imager. *Opt. Express*, 17:6368–6388, 2009.

[35] Y. Wang, N. P. Pitsianis, S. T. McCain, M. Gehm, and D. Brady. Coded apeture raman spectroscopy for quantitative measurements of ethanol in a tissue phantom. *Applied Spectroscopy*, 60:663 – 671, 2006.

[36] S. Wright, R. Nowak, and M. Figueiredo. Sparse reconstruction by separable approximation. *IEEE Transactions Signal Processing*, 57(8):2479–2493, 2009.

[37] Y. Wu, I. O. Mirza, G. R. Arce, and D. Prather. Development of a digital-micromirror-device-based multishot snapshot spectral imaging system. *Opt. Lett.*, 36(14):2692–2694, 2011.